

Holonomic quantum manipulation in the Weyl disk

Boogers, Victor; Erdmanis, Janis; Nazarov, Yuli

DOI

[10.1103/PhysRevB.105.235437](https://doi.org/10.1103/PhysRevB.105.235437)

Publication date

2022

Document Version

Final published version

Published in

Physical Review B

Citation (APA)

Boogers, V., Erdmanis, J., & Nazarov, Y. (2022). Holonomic quantum manipulation in the Weyl disk. *Physical Review B*, 105(23), Article 235437. <https://doi.org/10.1103/PhysRevB.105.235437>

Important note

To cite this publication, please use the final published version (if applicable). Please check the document version above.

Copyright

Other than for strictly personal use, it is not permitted to download, forward or distribute the text or part of it, without the consent of the author(s) and/or copyright holder(s), unless the work is under an open content license such as Creative Commons.

Takedown policy

Please contact us and provide details if you believe this document breaches copyrights. We will remove access to the work immediately and investigate your claim.

Holonomic quantum manipulation in the Weyl disk

Victor Boogers, Janis Erdmanis , and Yuli Nazarov*Kavli Institute of Nanoscience, Delft University of Technology, 2628 CJ Delft, The Netherlands*

(Received 10 July 2021; revised 30 May 2022; accepted 16 June 2022; published 27 June 2022)

It has been shown that a Weyl point in a superconducting nanostructure may give rise to a Weyl disk where two quantum states are almost degenerate in a two-dimensional manifold in the parametric space. This opens up the possibility of a holonomic quantum manipulation: A transformation of the wave function upon an adiabatic change of the parameters within the degenerate manifold. In this paper, we investigate in detail the opportunities for holonomic manipulation in Weyl disks. We compute the connection at the manifold in quasiclassical approximation to show it is Abelian and can be used for a phase gate. To provide a closed example of quantum manipulation that includes a state preparation and readout, we augment the holonomic gate with a change of parameters that brings the system out of the degenerate subspace. For numerical illustrations, we use a finite value of quasiclassical parameter and exact quantum dynamics. We investigate the fidelity of an example gate for different execution times. We evaluate the decoherence rate and show it can be made small to ensure a wide frequency range where an adiabatic manipulation remains coherent.

DOI: [10.1103/PhysRevB.105.235437](https://doi.org/10.1103/PhysRevB.105.235437)

I. INTRODUCTION

A quantum computer promises unprecedented advantage over a classical one for a set of challenging problems like protein folding [1] and prime number factorization [2]. However, building it is a challenge since it is necessary to isolate a set of quantum states from the environment as well as to manipulate it within the same environment. A particular obstacle is decoherence whereby the states pick up the fluctuations of the environment, which adds stochastic dynamical phases and may induce dissipation [3,4].

An alternative way to meet the challenge is the quantum manipulation within degenerate subspaces that have gained considerable interest nowadays [5–7]. The resonant manipulation that can be applied in the most systems with well-separated energy levels does not work for degenerate subspaces. Instead, the manipulation is performed within a degenerate manifold: A set of parameters within which the states are degenerate and distinct. An adiabatic change of parameters in time along a trajectory within this manifold corresponds to a unitary operator in the degenerate subspace, that depends on the trajectory rather than on the way it is traversed. Such mapping of a trajectory to a unitary operator for manifold is often characterized with a connection that sets how a wave function defined at a point is transported to other points in an infinitesimally small neighborhood. An important property of a connection is the holonomy: A property that transporting a vector over different trajectories with the same starting point and destination results in different vectors. This is the manifestation of either curvature of the connection or a singularity that separates the trajectories into topological classes, so that the transportation results differ only if two trajectories belong to different classes.

In quantum mechanics, the connection is characterized by a gauge potential [8], and the unitary operators correspond

to the path integrals involving the potential. They are called holonomic transformations. The advantage of using these transformations for wave-function manipulation is that in adiabatic limit the result is determined by the trajectory only, rather than by details of the time dependence of the parameter evolution along the trajectory. This provides the robustness against parametric noise and other decoherence sources.

In quantum mechanics, the connection of a manifold can be either Abelian or non-Abelian. The Abelian connection has been studied by Berry [9] while Wilczek and Zee [8] addressed the general non-Abelian case specific for degenerate manifolds. In general, a holonomic transformation is assigned to any curve in the Hilbert manifold. The transformations have been studied in the context of geometric phase [10] and nonadiabatic geometric computation [11–19]. For an Abelian connection, the unitary operators representing all trajectories with the same end points can be simultaneously diagonalized. Such diagonalization is not possible for a non-Abelian connection, and thus holonomy is irreducible. This in principle permits an implementation of a complete set of quantum gates to achieve universal holonomic quantum computation in a variety of systems [20]. However, the experimental realization of these schemes appeared difficult due to long execution times required to get rid of nonadiabatic corrections [11,21,22].

A particular example of holonomic manipulation involves a two-dimensional system of indistinguishable anyons. Changing the positions of the anyons provides a connection with a vanishing curvature [23]. The holonomic transformations are the same for all trajectories from the same homotopy class specified by number of windings around the anyons. This sets the paradigm of topological quantum computation [24]. Within the paradigm, a quantum manipulation is implemented as a braiding, a move of anyons along the trajectories whereby all anyons return to starting points making

loops around each other. The holonomic transformations in this case are robust against the fluctuations of the trajectory shapes; this promises to implement manipulations of an exceptional fidelity [25]. These opportunities have raised interest in anyonic excitations in solid-state systems such as Majorana superconductor-semiconductor nanowires [26] and specific fractional quantum Hall effect setups [27,28].

Many quantum systems exhibit topologically protected energy-level crossings in three-dimensional parameter space that are commonly called Weyl points [29]. In solid-state physics, the parameter space is a space of wave vectors confined to a Brillouin zone of the crystal lattice. The Weyl points in solid-state band structures are a subject of active theoretical and experimental research [30]. Another realization of Weyl points concerns a multiterminal superconducting nanostructure, where the Weyl points appear as the crossings of mirror-symmetric Andreev bound states at zero energy [31] in the parametric space of three independent superconducting phases.

It has been shown recently that the interaction effects can cause a substantial modification of Weyl points [32]. A generic interaction model combines soft confinement and fluctuations in the parameter space. In the quasiclassical limit, a *Weyl disk* is formed in the vicinity of a point: Two quantum states are (almost) degenerate in a finite two-dimensional (2D) region of the three-dimensional (3D) parameter space. The residual level splitting is exponentially small in the quasiclassical parameter. This makes the degeneracy physically achievable for a variety of systems. For instance, in a multiterminal superconducting junction, the Weyl disk can be realized by placing large inductances between each superconductor terminal and the nanostructure. This makes the phase differences at the nanostructure softly constrained by the phase differences at the terminals.

The degenerate manifold at Weyl disk may be used for holonomic quantum manipulation. We explore this opportunity in this paper. Using the quasiclassical approximation, we compute the connection at the Weyl disk to show it is Abelian. A corresponding quantum gate [Fig. 1(a)] is thus a phase gate in a proper basis. We show the relation of the phase shift and the Berry phase from the classic example of $\frac{1}{2}$ spin in magnetic field [9]. To demonstrate richer opportunities for quantum manipulation, we augment the purely holonomic transformations by adiabatic passages to the exterior of the disk [Fig. 1(b)]. We show that the crossing of the disk boundary corresponds to a Hadamard gate. With this, we provide a closed example of quantum manipulation that includes an initialization in a superposition state, a holonomic manipulation, and a subsequent readout. The crossings of the disk boundary can occur in different points as well [Fig. 1(c)]. The resulting gates are equivalent if a trajectory in the disk is closed along the boundary of the disk [cf. Figs. 1(c) and 1(d)]. We investigate the work of these quantum gates beyond the adiabatic approximation with a full numerical simulation at a finite and moderate value of the quasiclassical parameter. We evaluate the gate fidelity as function of the execution time and provide analysis of the dominant nonadiabatic corrections.

It has to be noted that the setup under consideration is not decoherence free. The fluctuations of control parameters that drive the system out of the degenerate subspace is the

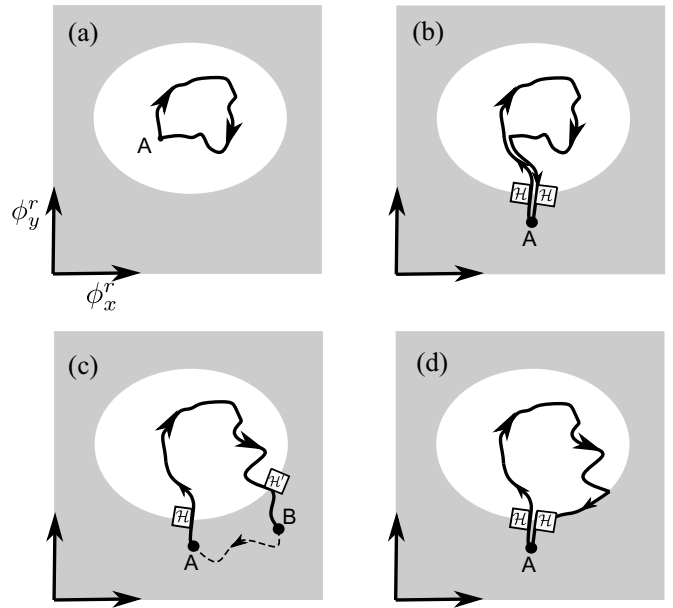


FIG. 1. A Weyl disk (shown in white) is a 2D elliptic region in the parametric space where two quantum states are degenerate. (a) A purely holonomic transformation is achieved by adiabatic change of parameters along a closed trajectory. (b) To achieve more functionality, we consider adiabatic passages beyond the degenerate manifold. A Hadamard gate describes the crossing of the disk boundary. (c) The crossings of the boundary do not have to be in the same point. (d) The gate from (c) is equivalent to the gate where the trajectory in the disk is closed along the disk boundary.

main source of decoherence. The execution times of the gates should be smaller than the decoherence time to achieve the coherent manipulation, although they should be long enough to satisfy the adiabaticity condition. We show how to minimize the decoherence rate to achieve this in a wide frequency range.

The paper is organized as follows. In Sec. II we provide a Hamiltonian description of a multiterminal superconducting junction with a Weyl point and discuss the soft constraints that enable the Weyl disk regime. In Sec. III we consider the Weyl disk manifold in quasiclassical approximation and supplement it with a numerical example at a finite and moderate quasiclassical parameter. Section IV is separated into subsections where we (A) recall the concept of holonomic transformations, (B) compute the connection in the quasiclassical limit, (C) consider the adiabatic passages beyond the disk, and (D) evaluate the connection beyond the quasiclassical limit. In Sec. V we analyze the deviations from adiabatic approximation, and present the results of the full quantum dynamics simulation evaluating the fidelity of the swap gate as function of the gate execution time. Section VI is devoted to the consideration of the decoherence. We conclude in Sec. VII.

II. THE SYSTEM

Weyl points in various physical systems have been a subject of an active research [29,30,33]. An important property of a Weyl point is its topological protection: The conservation of

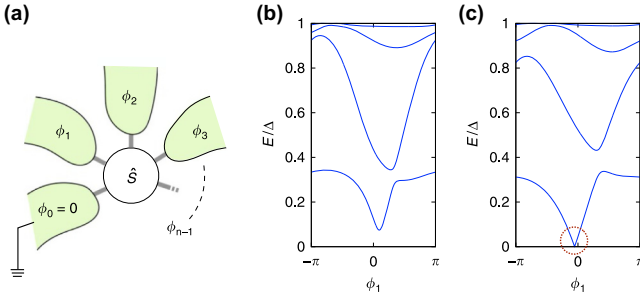


FIG. 2. (a) Multiterminal superconducting junction with superconducting phases ϕ_n . (b) The Andreev bound state spectrum as a function of one of the superconductor terminal phases ϕ_1 with the other phases at general settings. (c) The same spectrum for the choice of the other phases corresponding to a Weyl point at certain ϕ_1 [31].

topological charge guarantees that small perturbations of the system just shift rather than destroy the point and associated conical singularity in energy spectrum.

Recently, it was shown [31] that multiterminal superconducting junctions with the leads of ordinary topologically trivial material can host Weyl points. In other words, the lowest in energy Andreev bound state (ABS) can be tuned to zero energy (Fig. 2). The tuning parameters are the superconducting phases of the terminals. Owing to gauge invariance, only phase differences between terminals matter and thus at least four terminals are required to achieve Weyl points.

The Hamiltonian describing the conical spectrum in the vicinity of a Weyl point is a 2×2 matrix in the basis of two singlet degenerate ground states of the nanostructure [34]

$$H_{\text{WP}} = (\hbar/2e) \sum_{n=x,y,z} I_n \phi_n \hat{\sigma}_n. \quad (1)$$

Here, $\hat{\sigma}_n$ are the Pauli matrices in the space of the singlet states, ϕ_n are the superconducting phases counted from the positions, and I_n are the coefficients defining the energy slopes of the spectrum. The corresponding energy levels are $E = \pm(\hbar/2e)\sqrt{\sum_n I_n^2 \phi_n^2}$.

In a realistic setup, the multiterminal superconducting junction is embedded in a linear circuit (Fig. 3), and thus the phases determining the Weyl point become dynamical variables rather than parameters, $\phi_n \rightarrow \hat{\phi}_n$, and can deviate from the external phases ϕ_n^r that now play the role of control parameters. The linear circuit thus constrains softly the $\hat{\phi}_n$ to ϕ_n^r .

The constraint in general can be implemented as a quadratic addition to the energy. In particular, for our setup this is an inductive energy: Each inductance L_n adds a term $(\hbar/2e)^2(\hat{\phi}_n - \phi_n^r)^2/2L_n$ constraining the corresponding phase. The quantum fluctuations of the phase around this point are determined by the corresponding capacitances that provide charging energy $(2e\hat{N}_n)^2/2C_n$, \hat{N}_n being a variable canonically conjugated to $\hat{\phi}_n$. The full Hamiltonian of the system with a soft constraint reads as

$$H(\vec{\phi}^r) = H_{\text{WP}} + \left(\frac{\hbar}{2e}\right)^2 \sum_n \frac{(\hat{\phi}_n - \phi_n^r)^2}{2L_n} + \sum_n \frac{(2e\hat{N}_n)^2}{2C_n}, \quad (2)$$

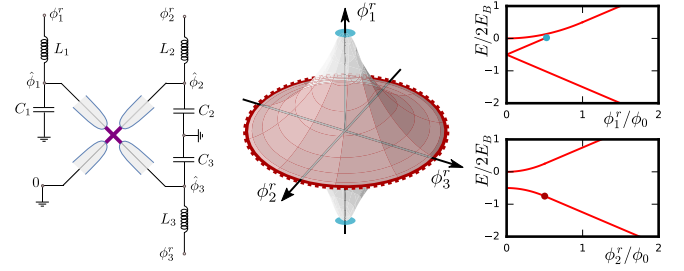


FIG. 3. Formation of the Weyl disk. Left: A four-terminal Josephson junction embedded in a linear circuit. The linear circuit represents the finite capacitances and inductances of the superconducting leads and the surrounding electromagnetic environment. Middle: The 3D region where the two minima of quasiclassical potential are present. The two minima are of the same energy at a 2D region shown in red: The Weyl disk. Right: The energy spectrum along a line perpendicular to the disk (upper panel) and one in the disk plane (lower panel). In upper panel, the energies of two lowest minima split upon increasing the distance from the disk plane. In lower panel, two minima are degenerate and merge in one at the disk edge (red dot in the plot) [32].

where the middle term accounts for the soft constraint and the last term for the fluctuations. This is a minimum model of the embedding linear circuit; more complex models involve general frequency-dependent response functions of the circuit and do not change the qualitative conclusions.

The relevant scales in this Hamiltonian can be understood when considering a single-dimension version of it:

$$H(\phi^r) = (\hbar/2e)I\phi\hat{\sigma}_z + \left(\frac{\hbar}{2e}\right)^2 \frac{(\hat{\phi} - \phi_n^r)^2}{2L} + \frac{(2e\hat{N})^2}{2C}. \quad (3)$$

The diagonalization of this Hamiltonian is trivial since the quasispin and ϕ separate and we have an oscillator centered at the positions that depend on the eigenvalue of spin $\sigma = \pm 1$, $\phi = \phi^r - \sigma\phi_0$, $\phi_0 \equiv 2eIL/\hbar$. At $\phi^r = 0$ these two positions correspond to degenerate minima separated by energy barrier $E_B = LI^2/2$. The energy spectrum is given by (m being the number of quanta in the oscillator)

$$E_{m,\sigma} = \hbar\omega(m + 1/2) + \frac{\hbar}{2e}I\phi^r\sigma - E_B, \quad (4)$$

where $\omega = \sqrt{LC}$ is the oscillator frequency.

We assess the significance of quantum fluctuations by comparing the barrier height and the energy quantum in the oscillator. We introduce a quasiclassical parameter:

$$Q = \frac{E_B}{\hbar\omega} = \frac{1}{2} \left(\frac{LIe}{\hbar}\right)^2 \frac{\hbar}{e^2 Z}, \quad (5)$$

$Z = \sqrt{L/C}$ being the characteristic impedance of the oscillator. Since $Ze^2/\hbar \simeq 10^{-2}$ for typical circuits, the parameter can be large even for relatively small inductances. If $Q \gg 1$, the system is in the quasiclassical regime and the overlap of the states in two minima is exponentially small. In the opposite limit $Q \ll 1$ the overlap is big and the effect of soft confinement can be treated perturbatively.

We see that for one-dimensional version of the Hamiltonian the energy levels retain conical singularity as far as their

dependence on $\vec{\phi}^r$ is concerned. Generally, one expects this to hold for the 3D case as well: The confinement would just renormalize the “velocities” $\partial E/\partial\phi_n$ defining the singularity. It has been discovered in [32] that there is an important exception from this general rule: For one of the directions (we will call it an easy axis and take it for z direction) the velocity remains finite while vanishing in the limit of large Q for two perpendicular directions. The easy direction is defined by the biggest energy barrier: $E_B^z \equiv L^z I_z^2/2 > E_B^x, E_B^y$.

Thereby a Weyl point in the presence of confinement and in the quasiclassical limit becomes a Weyl disk (see Fig. 3): Two energy levels remain degenerate within an ellipse in the ϕ_x^r - ϕ_y^r plane, the semiaxes being given by $(n = x, y)$

$$A_n = \frac{4e}{\hbar I_n} (E_B^z - E_B^n). \quad (6)$$

This is related to the existence of two potential minima in the vicinity of the Weyl point corresponding to two spin directions. In quasiclassical approximation, the corresponding wave functions do not overlap being localized near the minima.

It has been shown that the residual level splitting is exponentially small in the quasiclassical parameter. The approximate degeneracy in the Weyl disk is potentially interesting for quantum manipulation: That could allow a superposition of two degenerate states to evolve in time very slowly and enables holonomic manipulations of this superposition by changing ϕ_x^r, ϕ_y^r along a trajectory. In the next section, we will discuss in detail the properties of the states at the Weyl disk.

III. PROPERTIES OF THE STATES AT THE WEYL DISK

In this section, we complete and expand the analysis of the quantum states at the Weyl disk that was started in Ref. [32]. We present the numerical results and compare with the analytical ones in the quasiclassical limit. This analysis is crucial for understanding the available holonomic transformations and other manipulations at the manifold.

Let us first consider a numerical illustration (Fig. 4). We choose a moderate value of the quasiclassical parameter $Q = E_B^z/\hbar\omega_z = 5$ in the Hamiltonian (2). The barriers in x, y directions are lower and equal, $E_B^{x,y}/E_B = 1/3$. The corresponding oscillator frequencies are also the same, $\hbar\omega^{x,y} = E_B^{x,y}$; this suggests the circular symmetry of the setup with respect to rotations about z . The effective Q in this direction is thus $\simeq 1$. We will use this set of parameters for all numerical illustrations in the paper since it proves the feasibility of holonomic manipulations at moderate values of the quasiclassical parameter.

In the left panel and inset of Fig. 4, we present the energies of the four lowest states. We will perform quantum manipulations in the basis of the two lowest states. As we will see later in dynamical simulations, the wave function from this basis mostly leaks to the third and fourth states.

In the left panel, we plot the energies versus ϕ_x^r at $\phi_{z,y}^r = 0$, that is, in the disk plane. The energies of the two lowest states are apparently degenerate up to $\phi_x^r \simeq 0.5A_x$. Deep in the quasiclassical limit, they remain degenerate up to $\phi_x^r = A_x$. The moderate value of Q results in the residual splitting

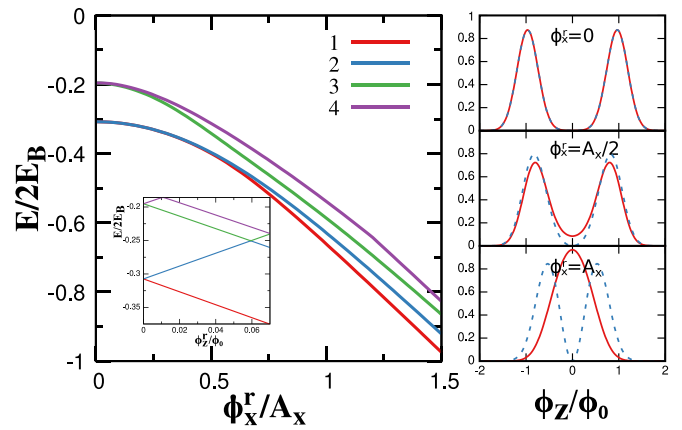


FIG. 4. Numerical results for the energy spectrum and wave functions. For numerical illustrations in this paper, we choose a moderate value of the quasiclassical parameter $Q = E_B/\hbar\omega_z = 5$ ($E_B \equiv E_B^z$). Other parameters are $\hbar\omega_{x,y}/E_B = \frac{1}{3}$, $E_B^{x,y}/E_B = \frac{1}{3}$. Left panel: Four lowest-energy levels of the Hamiltonian (2) in the disk plane $\phi_z^r = 0$ versus ϕ_x^r . The two lowest levels are degenerate deep in the disk. In the limit $Q \rightarrow \infty$ the degeneracy persists until the disk edge $(\phi_x^r)^2/A_x^2 + (\phi_y^r)^2/A_y^2 = 1$ with $A_{x,y}$ given by Eq. (6). Since $Q = 5$ is taken, the residual splitting at the disk edge is already comparable with $\omega_{x,y,z}$ which defines the energy distance to the higher levels. However, the splitting is not visible at $\phi_x^r < 0.5A_x$. Inset: Four lowest-energy levels versus ϕ_z^r at $\phi_{x,y}^r = 0$. The splitting is lifted upon a shift ϕ_z^r in the easy direction and is proportional to the shift. Right panel: The probability density of ϕ_z , $p(\phi_z) = \sum_\sigma \int |\Psi_\sigma|^2 d\phi_x d\phi_y$, in the disk plane for even (solid line) and odd (dashed line) lowest-energy states at several values of ϕ_x^r . The probability deep in the disk separates in two almost nonoverlapping peaks corresponding to two degenerate minima in the effective potential. At the edge of the disk, the minima merge resulting in a single peak.

that becomes comparable with the energy distance between the third and the second states at the edge of the disk.

It is important for further consideration to note a symmetry of the Hamiltonian at this choice of the parameters: It is invariant with respect to 180° rotation about the x axis. Owing to this, the splitting is diagonal in the basis of odd and even states with respect to the rotation. The first and the fourth state are even, while the second and third are odd.

If we change the phase in easy direction ϕ_z^r , the degeneracy is immediately lifted (inset of the Fig. 4), the splitting being proportional to ϕ_z^r . An instructive picture to comprehend this is that of a two-well potential depending on ϕ_z . The energies of the distinct potential minima are aligned in the disk plane and are shifted by ϕ_z^r in opposite directions. The distance between the minima reaches maximum at the center of the disk and decreases upon moving to the edge of the disk where two minima merge into one. In the quasiclassical limit, the wave function is localized at the minima. This is illustrated in the right panel of Fig. 4 where we plot the probability density $p(\phi_z)$ for even and odd states. We observe two distinct peaks at the center, slightly overlapping peaks at $\phi_x^r \simeq 0.5A_x$ and a single peak at the disk edge.

To characterize the double-well potential, we resort to quasiclassical approximation. If we neglect the quantum fluctuations completely, the quantum states are localized in

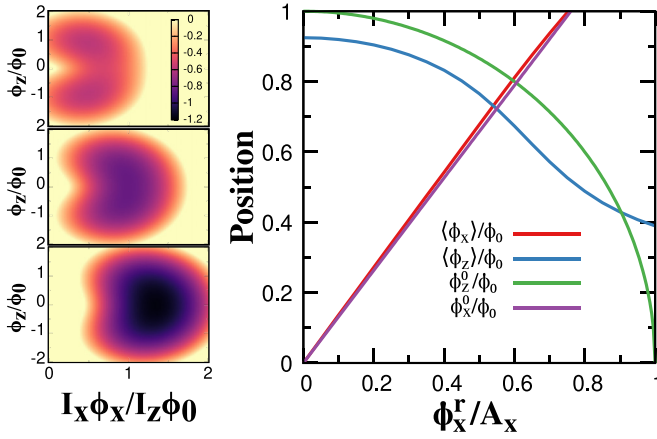


FIG. 5. The effective potential [Eq. (10)] and comparison with the numerical results. Left panel: Color contours of the quasiclassical effective potential in the ϕ_z - ϕ_x plane for the parameters at the Weyl disk: $\phi_z^r, \phi_y^r = 0$ and $\phi_x^r/A_x = 0.5, 1, 1.5$ from the upper to lower plots. The minima of this double-well potential merge at the disk edge. Right panel: The locations of the potential minima $\phi_{x,z}^0$ given by Eq. (11) and the numerical averages $\langle \phi_{x,z} \rangle$. To compute the averages, we take the wave functions of the two lowest states and arrange their superposition corresponding to the state localized in the upper minimum. The locations and averages are in reasonable agreement even for the moderate Q chosen.

superconductor phase space. The states can be decomposed as follows:

$$|\Psi\rangle = |\vec{\phi}\rangle \otimes |S\rangle, \quad (7)$$

where $|\vec{\phi}\rangle$ is a wave function with definite values of the superconducting phases and $|S\rangle$ is a two-component wave function in the spin space. This decomposition allows us to determine $|S\rangle$ from the Hamiltonian (2). Since we are looking for the states of the minimum energy, we set the spin to be antiparallel to the effective “magnetic field” at the point $\vec{\phi}$,

$$\vec{W} \cdot \vec{\sigma} |S\rangle = -|S\rangle, \quad (8)$$

\vec{W} being the normalized vector in the direction of the “field”

$$W_n = \frac{I_n \phi_n}{\sqrt{\sum_n I_n^2 \phi_n^2}}. \quad (9)$$

With this, we evaluate the effective potential for the state $|\psi\rangle$ averaging the Hamiltonian over the state (8) and neglecting the charging energy:

$$V(\vec{\phi}) = -\frac{\hbar}{2e} \sqrt{\sum_n I_n^2 \phi_n^2} + \left(\frac{\hbar}{2e}\right)^2 \sum_n \frac{(\phi_n - \phi_n^r)^2}{2L_n}. \quad (10)$$

In Fig. 5 (left) we plot the color contours of this effective potential in the ϕ_x - ϕ_z plane at three values of ϕ_x^r at $\phi_z^r, \phi_y^r = 0$. We see the minima moving towards each other upon increasing of ϕ_x^r and eventually merging at $\phi_x^r = A_x$. We expect the wave functions to be localized in the minima. To check for this, we compare the positions of the quasiclassical minima with the numerical averages $\langle \phi_{x,z} \rangle$ to find the reasonable correspondence even for the moderate Q .

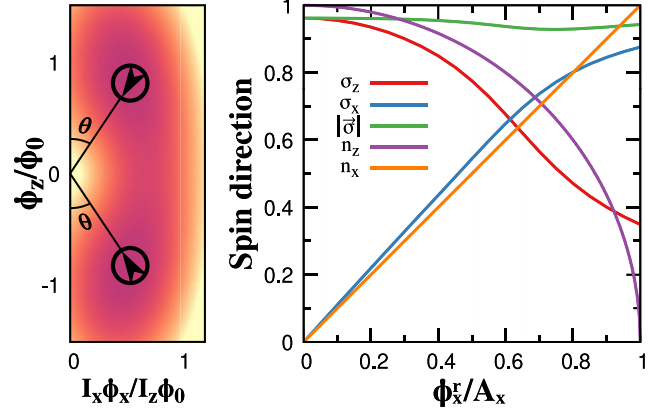


FIG. 6. The spin directions of the localized states compared with the numerical averages. Left panel: The contours of the even wave function. The spin directions in the potential minima are shown by the arrows. We rescaled the axes by A_x, A_z so that the spin directions point towards the origin. Right panel: The quasiclassical predictions for σ_x, σ_z as compared with the numerical averages for the superposition of two lowest eigenfunctions corresponding to the localization in the upper minimum. We show the quasiclassical spin direction \vec{n} with the spin direction obtained numerically. We normalize $\langle \vec{\sigma} \rangle$ to $\langle \vec{\sigma} \rangle^2 = 1$ to validate the decomposition given by Eq. (7). There is a good agreement even for the moderate Q taken.

The positions of the minima are given by [32]

$$\langle \hat{\phi}_x \rangle = \frac{\phi_0 I_z}{A_x I_x} \phi_x^r, \quad \langle \hat{\phi}_y \rangle = \frac{\phi_0 I_z}{A_y I_y} \phi_y^r,$$

$$\langle \hat{\phi}_z \rangle = \pm \phi_0 \sqrt{1 - \rho^2}, \quad (11)$$

where $\phi_0 = (2e/\hbar)I_z L_z$, $\rho^2 = (\phi_x^r)^2/A_x^2 + (\phi_y^r)^2/A_y^2$ ($\rho^2 = 1$ corresponds to the disk edge).

The locations of the minima determine the spin of the localized states. With Eqs. (8) and (11) we evaluate the angle θ it makes with the easy direction: $\cos \theta = \pm \langle \hat{\phi}_z \rangle / \phi_0$. The spins of two localized states in the center of the disk are aligned with z and are antiparallel. At the disk we come closer to the disk boundary, and the spins align with the disk plane and are parallel (see Fig. 6). The dependence of spin directions on $\vec{\phi}^r$ is essential for the holonomic transformations as discussed in the next section. To verify this numerically, we compute the average values of σ_x, σ_z for the superposition of the two lowest states that corresponds to the localization in the upper minimum. The results are presented in the right panel of Fig. 6. We see a reasonable agreement with the quasiclassical results that expectedly gets worse near the edge of the disk where the overlap of the states localized in different minima is significant.

IV. QUANTUM GATES

A. Geometric phase and holonomic transformations

Let us recall here the basics of geometric phase and holonomic transformations. We consider a Hamiltonian $\hat{H}(\vec{x})$ that depends on a set of parameters \vec{x} . We change the parameters in time along a trajectory $\vec{x}(t)$; this results in the time-dependent

Hamiltonian $\hat{H}(\vec{x})$. We introduce a local basis that diagonalizes $\hat{H}(\vec{x})$ in each point of parameter space,

$$E_n(\vec{x})|n\rangle = \hat{H}(\vec{x})|n\rangle. \quad (12)$$

The Schrödinger equation in the local basis reads as

$$i\hbar\dot{\psi}_n = E_n - \hbar\dot{x}_i M_{nm}^i \psi_m, \quad (13)$$

where the effective vector potential \hat{M}^i ,

$$M_{nm}^i = -i\langle n|\partial_i|m\rangle, \quad (14)$$

represents the connection of the bases. With this, and in general, the unitary transformation of the wave function can be separated into two parts [10]: The dynamical phase arising from the first term that represents the time-dependent energies, and a geometric phase arising from the second term that depends solely on the trajectory in the parametric space. The geometric phase is a phenomenon of potential importance for quantum information processing. There are setups where the dynamical phase can be neglected beyond the adiabatic approximation. Such examples have been actively studied in the field of nonadiabatic geometric quantum manipulation [11–18]. Alternatively, the trajectory in the parameter space can be passed adiabatically. The resulting geometric phase then reduces to a holonomic phase and is a basis of actively studied holonomic quantum manipulation [6,7].

The most common example of adiabatic manipulation is the Berry phase [9]. In this case, the energy levels are non-degenerate, and the adiabaticity implies that the frequencies associated with the parameter change are much smaller than the energy distances between the levels. One can neglect the nondiagonal elements of \hat{M}^i so the Schrödinger equation reduces to

$$i\hbar\dot{\psi}_n = E_n(\vec{x}(t))\psi_n - \hbar\dot{x}_i M_n^i \psi_n. \quad (15)$$

The dynamical phase separates from the geometric one. The latter depends on the trajectory only and is given by the line integral over the trajectory, \vec{x}_i, \vec{x}_f being the initial and final points of the trajectory:

$$\beta_n = \int_{\vec{x}_i}^{\vec{x}_f} \vec{M}_n \cdot d\vec{l} \quad (16)$$

The vector potential is not gauge invariant and changes upon a gauge transformation $|n\rangle \rightarrow U(\vec{x})|n\rangle$, $|U|^2 = 1$,

$$M_n^i \rightarrow M_n^i + U^* \partial_i U. \quad (17)$$

The gauge-invariant Berry phase is defined for closed trajectories $\vec{x}_i = \vec{x}_f$ and, by virtue of Stoke's theorem, equals to the surface integral of the curl of \vec{M} over the surface enclosed by the trajectory.

A fascinating extension of this concept pertains the case where several levels of the Hamiltonian are degenerate in a subspace of \vec{x} . The adiabaticity implies that the frequencies of the change are much smaller than the energy distance between the degenerate and nondegenerate levels. The adiabatic motion along a trajectory results in a unitary transformation in the degenerate subspace $\hat{S}(\vec{x}_i, \vec{x}_f)$:

$$\hat{S} = \mathcal{P} \exp \left(i \int_{\vec{x}_i}^{\vec{x}_f} \vec{M}(\vec{x}) \cdot d\vec{l} \right). \quad (18)$$

\mathcal{P} stands here for the ordering of \hat{M} along the trajectory. The operator vector potential is not invariant with respect to the unitary transformations of the basis $|n\rangle \rightarrow U(\vec{x})|n\rangle$, $|U|^2 = 1$,

$$M_n^i \rightarrow \hat{U}^\dagger M_n^i \hat{U} + \hat{U}^\dagger \partial_i \hat{U}. \quad (19)$$

The gauge invariance is achieved for closed trajectories, and pertains the eigenvalues of \hat{S} .

The holonomic transformations can be Abelian and non-Abelian. They are Abelian if $\hat{M}^i(\vec{x})$ can be chosen to commute for all \vec{x} . As we will see soon, this will be the case under consideration. The non-Abelian connection permits to realize a universal set of quantum gates [6,7] from holonomic transformations over different trajectories. However, the experimental implementation of them is difficult because of the nonadiabatic corrections [11,21,22].

B. Pure holonomic transformation

Let us apply these general considerations to the manifold of nearly degenerate wave functions at the Weyl disk. The first step is the parametrization of the basis in the degenerate subspace. We restrict ourselves to the deep quasiclassical limit. The natural basis choice is that of wave functions localized either in upper ($\phi_z > 0$) or lower ($\phi_z < 0$) minimum. As discussed, those can be decomposed into spin and orbital parts

$$|+\rangle = |S\rangle_+ |O\rangle_+; |-\rangle = |S\rangle_- |O\rangle_-. \quad (20)$$

Here, $|O\rangle_\pm$ are the normalized wave functions in $\vec{\phi}$ space located at the minima positions ($\langle \hat{\phi}_x \rangle, \langle \hat{\phi}_y \rangle, \pm\sqrt{1-\rho^2}$) [see Eq. (11)]. The $|S\rangle_\pm$ are spinors representing the spin antiparallel to the corresponding \vec{w}_\pm [see Eq. (9)], $\vec{w}_- = (w_+^x, w_+^y, -w_+^z)$.

The best choice of the coordinates in the elliptic disk corresponds to an unambiguous mapping of (ϕ_x^r, ϕ_y^r) to the upper hemisphere of the vector \vec{w}_+ . The two parametrizing angles θ, α , $0 < \theta < \pi/2$, $-\pi < \alpha < \pi$ are determined from

$$\sin \theta = \rho; e^{i\alpha} = \left(\frac{\phi_x^r}{A_x} + i \frac{\phi_y^r}{A_y} \right) \rho^{-1}; \quad (21)$$

while $\vec{w}_+ = (\cos \alpha \sin \theta, \sin \alpha \sin \theta, \cos \theta)$.

It is essential to choose $|S\rangle_\pm$ to ensure the continuity over the hemisphere and the absence of singularity. This is achieved by setting

$$|S\rangle_+ = \begin{bmatrix} -e^{-i\alpha} \sin \frac{\theta}{2} \\ \cos \frac{\theta}{2} \end{bmatrix}; |S\rangle_- = \begin{bmatrix} \cos \frac{\theta}{2} \\ -e^{i\alpha} \sin \frac{\theta}{2} \end{bmatrix}. \quad (22)$$

We compute the connection from Eq. (14). We may neglect the overlap between $|O\rangle_+$ and $|O\rangle_-$ in the quasiclassical limit, so the connection is diagonal in this basis and therefore Abelian. Moreover, the derivatives of $|O\rangle_\pm$ with respect to θ, α may be neglected as well. They give rise to the quantities proportional to the expectation values of the momentum and angular momentum for these states: Those are zero since the states are localized. The connection is thus determined by the derivatives of $|S\rangle_+$ and reads as

$$\hat{M}^\alpha = -\hat{\tau}_z \sin^2 \frac{\theta}{2}; \hat{M}^\theta = 0. \quad (23)$$

Thereby we reduce the situation to the classic example of Berry phase for an electron spin in spin magnetic field of constant amplitude [9]. Any holonomic transformation has a form of $\exp(-it_z\beta)$. This is a phase gate, whereby the states $|\pm\rangle$ acquire opposite phase shifts $\mp\beta$, β being the Berry phase from the example. For any closed trajectory, β is thus half of a solid angle enclosed by the trajectory on the hemisphere:

$$\beta = \oint \text{curl}\vec{M} dS = \frac{1}{2} \oint \sin\theta d\theta d\alpha. \quad (24)$$

In original coordinates, the connection and the curl read as follows:

$$M^x = \frac{\phi_y^r}{\rho^2 A_y A_x} (1 - \sqrt{1 - \rho^2}), \quad (25)$$

$$M^y = -\frac{\phi_x^r}{\rho^2 A_y A_x} (1 - \sqrt{1 - \rho^2}), \quad (26)$$

$$\text{curl}\vec{M} = \frac{1}{2A_x A_y \sqrt{1 - \rho^2}}. \quad (27)$$

We will consider the deviations due to finite Q in the Sec. IV D. In the next subsection, we will present quantum gates that enable measuring of the result of holonomic transformations.

C. Beyond the disk

The initialization and measurement of a quantum state at the degenerate manifold is questionable if ever possible in principle. To check if holonomic transformations work as supposed, we need to extend the quantum manipulation schemes. A simple way to achieve this would be to depart from the disk in easy direction. This leads to energy splitting between $|+\rangle$ and $|-\rangle$ and enables the measurement in this basis. However, with this measurement one cannot characterize the work of the phase gate predicted since it does not alter the probabilities to be in $|\pm\rangle$. Besides, the states almost do not overlap: This makes it difficult to arrange their superposition. We need to do something different.

We propose to augment the purely holonomic transformations in the disk with adiabatic passages in the same plane that go beyond the degenerate manifold (Fig. 1). This will bring us to the basis of the ground and first excited states that is continuous and unambiguous in the exterior of the disk. The adiabatic passages in the exterior change the phase difference between these basis states (mostly this is the effect of dynamical phase) not affecting the probabilities. Since the states are distinguishable (e.g., they correspond to different currents in the superconducting leads given by energy derivatives with respect to $\vec{\phi}$), these probabilities can be measured. Such measurements can be done with Andreev bound state spectroscopy [35–37]. The resonant quantum manipulation is also possible since the energies are split and the wave functions of the states overlap.

Let us find how the wave function is transformed between the interior and exterior bases upon crossing the disk boundary in the point $\theta = \pi/2$, $\alpha = \alpha_0$. We consider a transformation $R(\alpha_0)$: 180° rotation about the axis $(\cos\alpha_0, \sin\alpha_0, 0)$ that is in the direction of the spin-orientation vectors \vec{w}_\pm at this point. For a circular-symmetric disk $L_x = L_y$, $I_x = I_y$, $C_x = C_y$ this

is a true symmetry transformation of the Hamiltonian. For an anisotropic disk, this symmetry holds approximately in quasiclassical limit where the wave functions are concentrated near a point in $\vec{\phi}$ space.

The transformation should be diagonal in exterior basis. The ground and excited states are, respectively, even and odd upon $R(\alpha_0)$. As to the interior states, let us note that $|0\rangle_\pm = R(\alpha_0)|0\rangle_\mp$, so that

$$R(\alpha_0)|\pm\rangle = e^{\mp i\alpha_0}|\mp\rangle. \quad (28)$$

With this, we find that the wave functions in exterior and interior bases are related by a generalized Hadamard gate

$$\mathcal{H}(\alpha_0) \equiv \frac{1}{\sqrt{2}} \begin{bmatrix} 1 & e^{i\alpha_0} \\ e^{-i\alpha_0} & -1 \end{bmatrix}. \quad (29)$$

Since $\mathcal{H}^2 = 1$, the same matrix relates the bases upon the reverse passage.

Let us consider the quantum gate given in Fig. 1(b). We initialize the wave function in a point A beyond the disk: We can wait for the relaxation that brings the system to the ground state. After this, we can bring it to a superposition of the ground and excited states with a pulse of an oscillating $\vec{\phi}$ with the frequency matching the level splitting in this point. The adiabatic trajectory enters the disk, makes a loop there for a holonomic manipulation, and returns to the same point. The resulting quantum gate reads as

$$\hat{S} = \mathcal{H}(\alpha_0)e^{it_z\beta}\mathcal{H}(\alpha_0), \quad (30)$$

β being the Berry phase accumulated on the loop. This does not include the phase shifts in the exterior basis that do not change the probability. If we start in the ground or excited state, we end up in the excited or ground state with the probability

$$\mathcal{T} = \sin^2\beta. \quad (31)$$

Measuring these probabilities thus permits the characterization of the holonomic transformation. The answer for the probability, as expected, does not depend on the entrance point α_0 .

To measure the wave function in the exterior basis, one does not have to return to the initial point [Fig. 1(c)]: The measurement can be performed upon leaving the disk at some other point $(\pi/2, \alpha_1)$. The resulting quantum gate upon the phase factors in exterior basis is given by

$$\hat{S} = \mathcal{H}(\alpha_0)e^{-it_z\beta}\mathcal{H}(\alpha_1) \quad (32)$$

so the probability $\mathcal{T} = \sin^2[\beta^* + (\alpha_1 - \alpha_0)/2]$, β^* being the Berry phase acquired upon the part of the trajectory that connects the entrance and exit points. One may be surprised with the fact that β^* in principle is not gauge-invariant quantity. This is resolved if we note that in our gauge $(\alpha_1 - \alpha_0)/2$ is the Berry phase acquired upon a passage along the disk boundary from α_1 to α_0 . So, the gate in Fig. 1(c) is equivalent to that in Fig. 1(d) where the trajectory in the disk is closed. This restores the gauge-invariant expression $\mathcal{T} = \sin^2\beta$, β being the Berry phase accumulated along the closed trajectory.

More sophisticated gates can be arranged by entering and leaving the disk repeatedly along an adiabatic passage. They

are composed of Hadamard gates, holonomic phase shifts in interior basis, and dynamical phase shifts in exterior basis.

D. Connection beyond the quasiclassical limit

The simple expression for holonomic transformation obtained above is valid in the deep quasiclassical limit only and relies on the localization of the wave functions. One may wonder how accurate it is at finite values of Q . At first site, this problem is superfluous since finite values of Q give rise to the splitting of degenerate values in the disk; this formally invalidates the holonomic transformation. However, the splitting is exponentially small and may be neglected when the deviations from the deep quasiclassical limit are noticeable.

To investigate and illustrate this, in this section we compute numerically the connection at finite Q . We restrict ourselves to a simple particular case when this computation is straightforward: We concentrate on the circular trajectories at a circular-symmetric disk.

The circular symmetry of the disk implies $I_{x,y} = I_r$, $L_{x,y} = L_r$, $C_{x,y} = C_r$. Let us concentrate on a family of the Hamiltonians $\hat{H}(\alpha)$ along a circular trajectory $\phi_x^r = r \cos \alpha$, $\phi_y^r = r \sin \alpha$, r being the radius. This family is obtained by rotations about z axis by α ,

$$\hat{H}(\alpha) = R_z^{-1}(\alpha) \hat{H} R_z(\alpha), \quad (33)$$

where

$$R_z(\alpha) = \exp(-i\alpha \hat{J}_z) \quad (34)$$

and \hat{J}_z is the angular momentum operator. R_z^α represent rotation around easy direction with an angle α . The rotation thus generates the family of the bases diagonalizing $\hat{H}(\alpha)$:

$$|n\rangle_\alpha = \exp(-i\alpha \hat{J}_z) |n\rangle. \quad (35)$$

The connection \hat{M}^α is thus determined through the matrix elements of \hat{J}_z [see Eq. (14)], and is constant over the trajectory. One needs to diagonalize the Hamiltonian only once per trajectory to compute the connection.

We project \hat{J}_z on the two lowest eigenstates $|e\rangle$, $|g\rangle$, of the Hamiltonian

$$M_{ab}^\alpha = \langle a | \hat{J}_z | b \rangle, \quad (36)$$

where $a, b = g, e$. The half-difference of the eigenvalues of this matrix defines the holonomic transformation phase accumulated over the circular trajectory $\beta = \pi(M_+ - M_-)$.

One needs to take into account that the eigenvalues of \hat{J}_z are half-integer and the basis given by Eq. (35) is discontinuous. Owing to this, a formal calculation would give $\beta = \pi$ even at $r \rightarrow 0$ where no change of the Hamiltonian takes place. So, one has to subtract π to make sure $\beta \rightarrow 0$ at $r \rightarrow 0$.

The results are plotted in Fig. 7. In the deep quasiclassical limit, the angular momentum operator can be replaced with $\sigma_z/2$ and the holonomic phase is given by

$$\beta = \pi \frac{1 - \langle \hat{\sigma}_z \rangle}{2} = \pi(1 - \sqrt{1 - (r/A)^2}), \quad (37)$$

A being the disk radius. We observe significant corrections to the quasiclassical limit at finite Q : Those become bigger at the disk boundary and at the smaller Q . However, the overall dependence of $\beta(r)$ is preserved even at $Q = 4$.

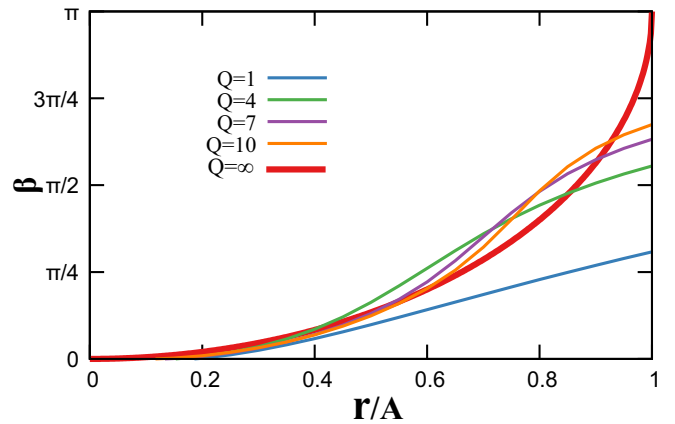


FIG. 7. Holonomic phase at various finite values of Q for a circular trajectory of radius r at the circular-symmetric disk. We compare it with the quasiclassical result [Eq. (37)] in the limit $Q \rightarrow \infty$.

V. QUANTUM DYNAMIC

In this section, we discuss the deviations from the ideal results of the execution of the quantum gates described. The deviations come from the residual level splitting in the disk and from the nonadiabatic excitations to higher levels in the course of the execution at finite time. We illustrate these sources with the numerical examples of the quantum dynamics of the full Hamiltonian (2). The parameters of the Hamiltonian used for illustrations are the same as in the previous sections corresponding to the moderate quasiclassical parameter Q and circular symmetry. We show that the gates work well even in this case.

We concentrate on the gate of the type given in Fig. 1(c). We chose a simple family of the trajectories (Fig. 8) consisting of two straight passages (“arms”) in radial direction and an arc around the origin. The initial and final points A, B are beyond the disk at the same distance $R > A$ from the origin, A being the disk radius. The radius and the angle of the arc are r and Θ , respectively. We expect the holonomic phase β to accumulate upon the passage

$$\beta = \frac{1}{2} \Theta \sqrt{1 - \left(\frac{r}{A}\right)^2}. \quad (38)$$

The time dependence of $\vec{\phi}^r$ at the trajectory can be defined in terms of the angular velocity Ω at the arc part and the linear

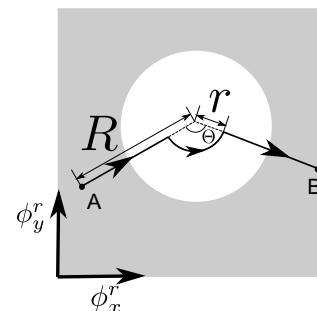


FIG. 8. The concrete example trajectories investigated in Sec. V.

velocity $v \equiv A\dot{\rho}$. The overall execution time of the gate is thus $T = \Theta/\Omega + 2(R-r)/v$. In a realistic manipulation, it is easy to make these velocities time dependent, preserving the total execution time; this might be a possibility to reduce the nonadiabatic corrections and thus improve the gate performance. However, the qualitative analysis made and our attempts of such optimization did not show any substantial improvement. The optimal time dependence of the velocities is close to constant.

We consider the deviations at the arc part and at the arms separately, and conclude by combining both in an example of the gate fidelity versus the execution time T . The Schrödinger equation at the arc part is best expressed in the local basis (35),

$$i\hbar\dot{\psi}_n = E_n\psi_n - \hbar\Omega(t)J_{nm}^z\psi_m, \quad (39)$$

the effective Hamiltonian not depending on time if $\Omega(t) = \text{const}$. The initial condition corresponds to the wave function localized in the two lowest levels $\psi_{1,2} \neq 0$, and the equation needs to be solved at the time interval $(0, \Theta/\Omega)$.

The first source of the deviations is the residual level splitting $E_2 - E_1$. The proper work of the holonomic gate requires this splitting to be smaller than the second term $\propto \Omega$, that is, $|E_2 - E_1| \ll \hbar\Omega$. If this condition is fulfilled, the deviations in probabilities are proportional to $[(E_2 - E_1)/\hbar\Omega]^2$.

The second source are the nonadiabatic corrections corresponding to the excitations to higher levels $n > 2$. The probabilities of the excitations from the states $|1\rangle, |2\rangle$ can be estimated as

$$P_{1,2 \rightarrow n} \approx |\langle n | \hat{J}_z | 1, 2 \rangle|^2 \left(\frac{\hbar\Omega}{E_n - E_{1,2}} \right)^2. \quad (40)$$

The small probabilities thus require $\hbar\Omega \ll |E_n - E_{1,2}| \simeq \hbar\omega_{x,y,z}$. The execution time thus should be much larger than $\omega_{x,y,z}^{-1}$.

We illustrate this with the quantum dynamics simulation at the arc part of the trajectory (Fig. 9). We simulate the work of the gate assuming its ideal execution while passing the arms. The initial state corresponds to the excited state in the exterior basis at the point A. We compute the probabilities $P_{1,2}$ to end up in the ground and excited states at the point B. For an ideal gate, those are given by $P_{1,2} = \sin^2 \beta, \cos^2 \beta$.

We plot the probabilities versus Θ for three different angular velocities $\Omega = 10^{-2}, 10^{-1}, 10^0\omega_z$. We choose $r = 0.25$ where the residual splitting $E_2 - E_1 = 0.002\omega_z$. At the smallest Ω , the deviation owing to the residual splitting is noticeable. There is no excitation to the higher levels, so that $P_1 + P_2 = 1$. At the intermediate Ω , the results follow those of the ideal gate with the numerical accuracy. The probabilities achieve minimum or maximum at $\Theta \approx \pi/1.03$ corresponding to $\beta = \pi/2$. At the highest Ω , the nonadiabatic correction becomes noticeable. The probability progressively leaks to higher levels, with only a half of it remaining in the computational subspace for the longest gate $\Theta = 2\pi$. Despite the significant deviations, the curves at the lowest and at the highest angular velocity still follow the oscillatory pattern. This demonstrates that the gate works in a wide range of the angular velocities.

Let us analyze the deviations coming from the radial arms of the trajectory. The residual splitting in this case only modifies the phase factor in the exterior basis and can be

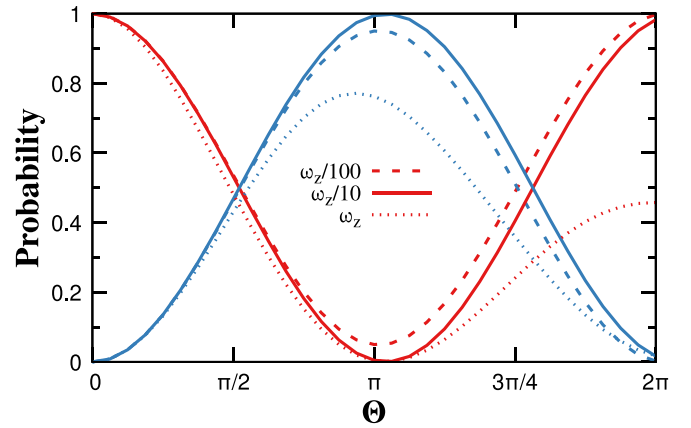


FIG. 9. The deviations coming from the arc part. We assume the ideal gate work at the arms of the trajectory. The initial state is an excited state $|2\rangle$ in the exterior basis. We plot the probabilities $P_{1,2}$ (blue and red) versus Θ at three different angular velocities $\Omega = 10^{-3}, 10^{-2}, 10^{-1}\omega_z$ (dashed, solid, and dotted lines). At the intermediate Ω , the results coincide with those for the ideal gate upon numerical accuracy. At the smallest Ω , the deviations are due to the residual level splitting in the disk interior. At the highest Ω , the deviations are due to nonadiabatic excitation to the higher levels.

disregarded. To quantify the nonadiabatic corrections, we represent the Schrödinger equation in the instantaneous basis $H(t)|n(t)\rangle = E(t)|n(t)\rangle$ and compute the probabilities to be in the excited states $n > 2$ in the second-order perturbation theory in terms of the nondiagonal elements of $\partial H/\partial t$.

Owing to circular symmetry, the results do not depend on the direction of the arm. We can compute the amplitudes for the motion in the x direction with the velocity depending on the actual value of $\phi_x^r, \dot{\phi}_x^r(\phi_x^r)$. The amplitude in the excited state n accumulated in the course of motion from r to R then reads as

$$\psi_n(R) = -\frac{\hbar I_x}{2e} \int_r^R ds_2 \frac{|\langle n(s_2) | \sigma_x | a(s_2) \rangle|}{E_n(s_2) - E_a(s_2)} \times \exp \left[\frac{i}{\hbar} \int_r^{s_2} \frac{1}{\dot{\phi}_x^r(s_1)} [E_n(s_1) - E_a(s_1)] ds_1 \right], \quad (41)$$

where $|a\rangle$ is a state from the computational subspace, either ground one or excited one.

To evaluate this integral numerically, we use instantaneous eigenstates obtained by diagonalization of the Hamiltonian at various ϕ_x^r . We summarize the results in Fig. 10 where we present the probability $1 \rightarrow 3$ versus the average velocity at the arm. The nondiagonal matrix element energizing the transition is plotted versus ϕ_x^r in Fig. 10(a). We try a family of ϕ_x^r dependencies of this velocity parametrized by γ :

$$\frac{\dot{\phi}_x^r(\phi_x^r)}{(\phi_x^r)} = \frac{\gamma}{2 \tanh(\gamma/2)} [1 - \rho^2 \tanh^2(\gamma/2)], \quad (42)$$

where $\rho = (2\phi_x^r - R - r)/(R - r)$. These velocity profiles are plotted in Fig. 10(b) for several values of γ . In the main figure, we plot the excitation probability versus the average velocity for several γ . The overall dependence is qualitatively consistent with exponential suppression of the transitions at low velocities, $\ln P \simeq v^{-1}$. The detailed dependence is not

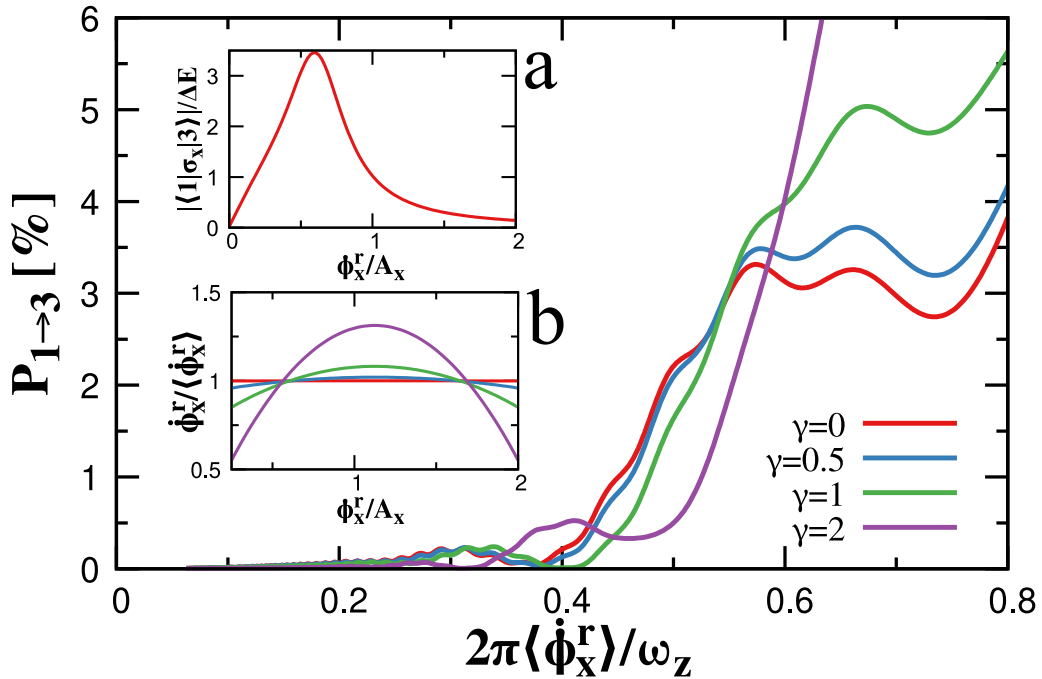


FIG. 10. The deviations coming from the radial part of the trajectory. The probability of the dominant excitation $P_{1 \rightarrow 3}$. For this example, the trajectory starts at $r = 0.25A$ and ends at $R = 2A$. (a) The intensity of the matrix element energizing the transition versus the distance from the origin ϕ_x^r . (b) The velocity profiles corresponding to Eq. (42). The curves correspond to various γ shown in the labels. Main figure: We plot the probability for various velocity profiles (γ is shown in the curve labels) as function of the average velocity. The probabilities are lower than 0.005 for lower velocities $< 0.06A\omega_z$ and increase rapidly at higher velocities. The slowest growth corresponds to the constant velocity profile $\gamma = 0$.

smooth, and the probabilities oscillate showing interference due to finite length of the arm. At all velocity profiles checked, the probabilities are $< 5 \times 10^3$ for $\dot{\phi}_x^r \approx A\omega_z/4\pi$ and grow rapidly at higher velocities. We find that the time-independent velocity profile $\gamma = 0$ eventually provides smaller probabilities and is thus advantageous for the gate design.

We illustrate the deviations on all parts of the trajectory by computing the fidelity of the swap gate versus the execution time (Fig. 11). A swap gate implements the transformation $|1\rangle \rightarrow |2\rangle$; $|2\rangle \rightarrow |1\rangle$ in the exterior basis, that is, $\mathcal{T} = 1$. The

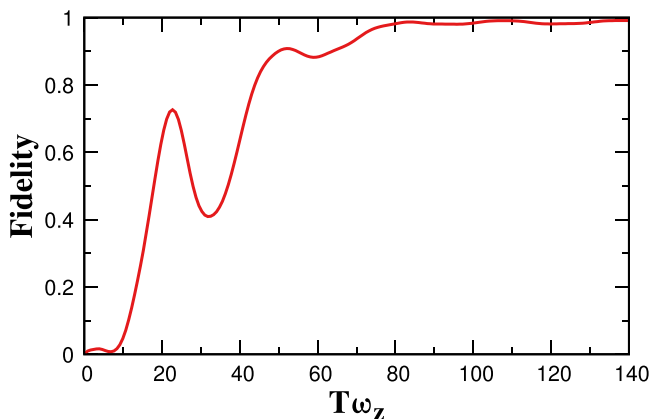


FIG. 11. The fidelity of the holonomic swap gate as function of the execution time T . The gate corresponds to the trajectory with $r = 0.25A$, $R = 2A$, $\Theta = \pi$ and is executed with constant velocity along the trajectory.

actual example differs a bit from the swap gate: The trajectory parameters are $r = 0.25A$, $R = 2A$, $\Theta = \pi$; this corresponds to $\beta \approx 1.5209$ that differs slightly from the swap gate value of $\pi/2$. However, $\mathcal{T} \approx 0.9975$ for this value of β so the difference with the ideal swap gate is negligible. The velocity in $\phi_x^r - \phi_y^r$ is constant along all parts of the trajectory. The fidelity is almost zero at $T\omega_z < 10$, increases nonmonotonically until $T\omega_z < 80$, and is close to ideal value at bigger T . We thus expect the gate to work good at $T\omega_z \simeq 100$ and longer. This looks parametrically bigger than a naive *ad hoc* estimation $T\omega_z \simeq 1$. However, we have to take into account that the typical energy differences along the path are $\simeq 0.2\omega_z$ and the better estimation for time is a period rather than the inverse frequency. So that $T\omega_z \simeq 100$ corresponds to 3–4 typical oscillation periods. Eventually, this corresponds to the number of peaks seen in the time dependence of the fidelity.

In the figure, we show a full numerical simulation of the swap gate for different runtimes. As expected from small runtimes, the execution is diabatic and thus all state probabilities after execution are close to zero. On the other hand, at long runtime limit, we see that the gate is relatively stable, a desirable property for holonomic computation.

VI. DECOHERENCE

In this section, we evaluate the decoherence time for Weyl disk under consideration and its effect on the work of the gates described. The most prominent decoherence mechanism is due to the fluctuations of the control phases that drive the system away from the 2D degenerate

manifold. Indeed, these fluctuations induce the time-dependent stochastic energy splitting of two degenerate states. This ruins the superposition of the states centered in different wells at $\phi_z \pm \phi_0\sqrt{1-\rho^2}$ [see Eq. (11)].

To derive the Hamiltonian describing the decoherence, we add to the Hamiltonian (2) the fluctuations of the relevant control parameter $\phi_z^r, \phi_z^i \rightarrow \phi_z^r + \hat{f}(t)$, concentrate on the terms linear in \hat{f} , and project then on the basis of the degenerate states. This yields

$$H_{\text{dec}} = -\left(\frac{\hbar}{2e}\right)^2 \frac{\phi_0\sqrt{1-\rho^2}}{L_z} \tau_z \hat{f}(t). \quad (43)$$

We can deduce already from this that the decoherence rate depends on the position at the disk. Since the fluctuation intensity does not depend on the position, the dependence of the rate is determined by the square of the prefactor in H_{dec} and is proportional to $1-\rho^2$ vanishing at the disk edges.

Let us develop a reasonable model for the fluctuations \hat{f} . For this, we have to soften the constraint on ϕ_z^r making it a dynamical variable in an electric circuit, that is, to repeat the procedure to soften the constraints on the original phases of the Josephson junction. With this, the spectrum of the fluctuations is expressed via the corresponding susceptibility $\chi(\omega)$ of the circuit and the temperature T :

$$\langle f_\omega^2 \rangle = \hbar \coth\left(\frac{\hbar\omega}{2k_B T}\right) \text{Im}\chi(\omega). \quad (44)$$

A realistic circuit model would include an inductance $L_1 \simeq L_z$ and a dissipative element, a resistor R in parallel with this inductance. The dissipative part of the susceptibility then reads as

$$\text{Im}\chi(\omega) = \frac{\omega L_1^2}{R[1 + (\omega L_1/R)^2]}. \quad (45)$$

Since the decoherence rate is supposed to be smaller than the temperature in frequency units, and the relaxation rate R/L_1 , the decoherence is determined by low-frequency fluctuations, and $\hat{f}(t)$ can be treated as a classical white noise. Collecting all the factors, we obtain for the decoherence rate

$$\frac{1}{\tau_d} = \phi_0^2 (1-\rho^2) k_B T \frac{L_1^2}{e^2 R L_z^2}. \quad (46)$$

It can be made small by increasing the load resistance R . This estimation should be taken with caution since at finite frequencies the load resistance can be shunted by the capacitive response in which case a common estimation for the resistor value is the vacuum impedance. The validity of Eq. (46) is ensured if the capacitive response is negligible at frequencies $\simeq \tau_d^{-1}$.

This rate has to be compared with the frequency scale ω_z below which the adiabatic manipulation is plausible. It is convenient to express ω_z in terms of the energy barrier and the quasiclassical parameter Q , $\hbar\omega_z = L_z I_z^2 / 2Q$. With this, the result of comparison does not depend on the Weyl point parameter I_z , and reads as

$$\frac{1}{\tau_d \omega_z} = \frac{8 k_B T L_1^2 Q}{\hbar R L_z} (1-\rho^2). \quad (47)$$

This number defines the range of frequencies available for coherent adiabatic manipulation and should be at least a couple of orders of magnitude smaller than one for successful

experiments. This can be achieved at sufficiently low temperatures and big resistances. For a realistic example, we choose $T = 10$ mK, $L_1^2/L = 2 \times 10^{-13} H$ (micrometer loop scale), very big quasiclassical factor $Q = 50$, and $R = 1$ kOhm. For this choice,

$$\frac{1}{\tau_d \omega_z} = 10^{-4}, \quad (48)$$

in the center of the disk implying that the coherent adiabatic manipulation is plausible within the four orders of magnitude wide frequency range.

The effect of the decoherence is incorporated to the evolution equation for the density matrix as an extra term next to the Hamiltonian dynamics

$$\frac{d\hat{\rho}}{dt} = -\frac{1}{2\tau_d(t)}(\hat{\rho} - \tau_z \hat{\rho} \tau_z). \quad (49)$$

Here, the time dependence of τ_d is determined by the current position $(\phi_x^r(t), \phi_y^r(t))$ on the manipulation path according to Eq. (46). The effect of the unitary gate $\exp(i\tau_z \beta)$ of the execution time t is given by

$$\rho_{++}^{(f)} = \rho_{++}^{(i)}; \quad \rho_{--}^{(f)} = \rho_{--}^{(i)}, \quad (50)$$

$$\rho_{+-}^{(f)} = e^{i\beta} X(t) \rho_{+-}^{(i)}; \quad \rho_{-+}^{(f)} = e^{-i\beta} X(t) \rho_{-+}^{(i)}; \quad (51)$$

$$dX/dt = -X/\tau_d(t), \quad (52)$$

where $\hat{\rho}^{(i/f)}$ is the density matrix before and after the execution. The effect of the decoherence is an exponential damping of the nondiagonal matrix elements $X(t) = \exp(-t/\tau_d)$ if the decoherence does not depend on time. Since it generally depends on the path, the resulting nonunitary gate does depend on the path in addition to the execution time dependence.

As explained, we expect the highest decoherence in the case of traversing the disk. The decoherence while moving beyond the disk is strongly reduced since the degenerate levels are split, and we may disregard this effect.

VII. CONCLUSIONS

In conclusion, we have investigated holonomic manipulations that can be performed utilizing approximate degeneracy at the Weyl disk: A rather counterintuitive example of 2D finite degenerate manifold in 3D parameter space. The Weyl disks can be realized by soft confinement of parameters in the superconducting nanostructures hosting the Weyl points in the spectrum of Andreev bound states, which is the example considered here. The resulting Hamiltonian is, however, generic and can be realized in many quantum systems with the Weyl-type crossings in the spectrum of discrete energy states, so our results are of general nature.

We have computed the connection in the Weyl disk manifold in the quasiclassical limit and found it Abelian: It realizes a phase gate, the phase difference being related to the Berry phase in its classic example. This may seem a rather discouraging result. However, we propose to augment the purely holonomic transformations with the adiabatic passages beyond the degenerate manifold. With this, we can propose the realization of more sophisticated gates and practical measurement of the results of the holonomic transformations.

We did quantum dynamic simulation of the gates proposed for realistic Hamiltonians and find they can work properly at rather short execution times. The execution time of the gate, despite being adiabatic, should be smaller than the decoherence time. We have computed decoherence rate for the dominant mechanism: The fluctuations of the control parameter along the easy axis that drive the system out of the degenerate 2D subspace. We have discussed how the decoherence modifies the result of a gate operation.

A natural continuation of this research line would include the consideration of several Weyl points brought into soft

confinement and interaction with each other. They would give rise to degenerate manifolds of higher dimensions with richer holonomic transformations and perhaps provide the protection against decoherence.

ACKNOWLEDGMENTS

This research was supported by the European Research Council (ERC) under the European Union's Horizon 2020 research and innovation programme (Grant Agreement No. 694272).

-
- [1] D. Wecker, B. Bauer, B. K. Clark, M. B. Hastings, and M. Troyer, Gate-count estimates for performing quantum chemistry on small quantum computers, *Phys. Rev. A* **90**, 022305 (2014).
- [2] P. W. Shor, Polynomial-time algorithms for prime factorization and discrete logarithms on a quantum computer, *SIAM Rev.* **41**, 303 (1999).
- [3] C. H. Bennett and D. P. DiVincenzo, Quantum information and computation, *Nature (London)* **404**, 247 (2000).
- [4] M. A. Nielsen and I. L. Chuang, *Quantum Computation and Quantum Information* (Cambridge University Press, Cambridge, 2009).
- [5] P. Zanardi and M. Rasetti, Holonomic quantum computation, *Phys. Lett. A* **264**, 94 (1999).
- [6] A. C. M. Carollo and V. Vedral, *Holonomic Quantum Computation* (Wiley, Hoboken, NJ, 2016), pp. 475–482.
- [7] L.-A. Wu, P. Zanardi, and D. A. Lidar, Holonomic Quantum Computation in Decoherence-Free Subspaces, *Phys. Rev. Lett.* **95**, 130501 (2005).
- [8] F. Wilczek and A. Zee, Appearance of Gauge Structure in Simple Dynamical Systems, *Phys. Rev. Lett.* **52**, 2111 (1984).
- [9] M. V. Berry, Quantal phase factors accompanying adiabatic changes, *Proc. R. Soc. London, Ser. A* **392**, 45 (1984).
- [10] Y. Aharonov and J. Anandan, Phase Change During a Cyclic Quantum Evolution, *Phys. Rev. Lett.* **58**, 1593 (1987).
- [11] E. Sjöqvist, D. M. Tong, L. M. Andersson, B. Hessmo, M. Johansson, and K. Singh, Non-adiabatic holonomic quantum computation, *New J. Phys.* **14**, 103035 (2012).
- [12] R. Leone, On the parallel transport in quantum mechanics with an application to three-state systems, [arXiv:1903.04928](https://arxiv.org/abs/1903.04928).
- [13] A. A. A. Jr, J. M. Fink, K. Juliusson, M. Pechal, S. Berger, A. Wallraff, and S. Filipp, Experimental realization of non-abelian non-adiabatic geometric gates, *Nature (London)* **496**, 482 (2013).
- [14] S. E. Economou and T. L. Reinecke, Theory of Fast Optical Spin Rotation in a Quantum Dot Based on Geometric Phases and Trapped States, *Phys. Rev. Lett.* **99**, 217401 (2007).
- [15] H. Li, Y. Liu, and G. Long, Experimental realization of single-shot nonadiabatic holonomic gates in nuclear spins, *Sci. China Phys. Mech. Astron.* **60**, 080311 (2017).
- [16] S.-L. Zhu and Z. D. Wang, Implementation of Universal Quantum Gates Based on Nonadiabatic Geometric Phases, *Phys. Rev. Lett.* **89**, 097902 (2002).
- [17] K. Nagata, K. Kuramitani, Y. Sekiguchi, and H. Kosaka, Universal holonomic quantum gates over geometric spin qubits with polarised microwaves, *Nat. Commun.* **9**, 9 (2018).
- [18] L.-M. Duan, Geometric manipulation of trapped ions for quantum computation, *Science* **292**, 1695 (2001).
- [19] P. Solinas, P. Zanardi, N. Zanghì, and F. Rossi, Semiconductor-based geometrical quantum gates, *Phys. Rev. B* **67**, 121307(R) (2003).
- [20] L. Faoro, J. Siewert, and R. Fazio, Non-Abelian Holonomies, Charge Pumping, and Quantum Computation with Josephson Junctions, *Phys. Rev. Lett.* **90**, 028301 (2003).
- [21] D. Parodi, M. Sassetti, P. Solinas, P. Zanardi, and N. Zanghì, Fidelity optimization for holonomic quantum gates in dissipative environments, *Phys. Rev. A* **73**, 052304 (2006).
- [22] K. Toyoda, K. Uchida, A. Noguchi, S. Haze, and S. Urabe, Realization of holonomic single-qubit operations, *Phys. Rev. A* **87**, 052307 (2013).
- [23] J. M. Leinaas and J. Myrheim, On the theory of identical particles, *Il Nuovo Cimento B Series 11* **37**, 1 (1977).
- [24] A. Kitaev, Fault-tolerant quantum computation by anyons, *Ann. Phys.* **303**, 2 (2003).
- [25] G. P. Collins, Computing with quantum knots, *Sci. Am.* **294**, 56 (2006).
- [26] J. D. Bommer, H. Zhang, Önder Gül, B. Nijholt, M. Wimmer, F. N. Rybakov, J. Garaud, D. Rodic, E. Babaev, M. Troyer, D. Car, S. R. Plissard, E. P. Bakkers, K. Watanabe, T. Taniguchi, and L. P. Kouwenhoven, Spin-Orbit Protection of Induced Superconductivity in Majorana Nanowires, *Phys. Rev. Lett.* **122**, 187702 (2019).
- [27] D. E. Feldman, The smallest particle collider, *Science* **368**, 131 (2020).
- [28] J. Nakamura, S. Liang, G. C. Gardner, and M. J. Manfra, Direct observation of anyonic braiding statistics, *Nat. Phys.* **16**, 931 (2020).
- [29] C. Herring, Accidental degeneracy in the energy bands of crystals, *Phys. Rev.* **52**, 365 (1937).
- [30] B. Yan and C. Felser, Topological materials: Weyl semimetals, *Annu. Rev. Condens. Matter Phys.* **8**, 337 (2017).
- [31] R.-P. Riwar, M. Houzet, J. S. Meyer, and Y. V. Nazarov, Multi-terminal Josephson junctions as topological matter, *Nat. Commun.* **7**, 11167 (2016).
- [32] J. Erdmanis, Á. Lukács, and Y. V. Nazarov, Weyl disks: Theoretical prediction, *Phys. Rev. B* **98**, 241105(R) (2018).

- [33] T. O'Brien, Applications of topology to Weyl semimetals and quantum computing, Ph.D. thesis, Leiden University, 2019.
- [34] T. Yokoyama and Y. V. Nazarov, Singularities in the Andreev spectrum of a multiterminal Josephson junction, *Phys. Rev. B* **92**, 155437 (2015).
- [35] A. Zazunov, V. S. Shumeiko, E. N. Bratus', J. Lantz, and G. Wendin, Andreev Level Qubit, *Phys. Rev. Lett.* **90**, 087003 (2003).
- [36] S. Shafranjuk, I. Nevirkovets, and J. Ketterson, A qubit device based on manipulations of Andreev bound states in double-barrier Josephson junctions, *Solid State Commun.* **121**, 457 (2002).
- [37] C. Janvier, L. Tosi, L. Bretheau, Ç. O. Girit, M. Stern, P. Bertet, P. Joyez, D. Vion, D. Esteve, M. F. Goffman, H. Pothier, and C. Urbina, Coherent manipulation of Andreev states in superconducting atomic contacts, *Science* **349**, 1199 (2015).